

UniDiff: Parameter-Efficient Adaptation of Diffusion Models for Land Cover Classification with Multi-Modal Remotely Sensed Imagery and Sparse Annotations

Yuzhen Hu
University of Houston
Houston, TX, USA
yhu34@uh.edu

Saurabh Prasad
University of Houston
Houston, TX, USA
saurabh.prasad@ieee.org

Abstract

Sparse annotations fundamentally constrain multimodal remote sensing: even recent state-of-the-art supervised methods such as MSFMamba are limited by the availability of labeled data, restricting their practical deployment despite architectural advances. ImageNet-pretrained models provide rich visual representations, but adapting them to heterogeneous modalities such as hyperspectral imaging (HSI) and synthetic aperture radar (SAR) without large labeled datasets remains challenging. We propose UniDiff, a parameter-efficient framework that adapts a single ImageNet-pretrained diffusion model to multiple sensing modalities using only target-domain data. UniDiff combines FiLM-based timestep-modality conditioning, parameter-efficient adaptation of approximately 5% of parameters, and pseudo-RGB anchoring to preserve pre-trained representations and prevent catastrophic forgetting. This design enables effective feature extraction from remote sensing data under sparse annotations. Our results with two established multi-modal benchmarking datasets demonstrate that unsupervised adaptation of a pre-trained diffusion model effectively mitigates annotation constraints and achieves effective fusion of multi-modal remotely sensed data.

1. Introduction

Dense pixel-level land-cover classification is a critical computer vision challenge with profound societal impact, enabling global climate monitoring, precision agriculture, disaster response, and urban planning at unprecedented scales. However, the high cost of pixel-level annotations severely limits the practicality of fully supervised multimodal fusion approaches at scale. Remote sensing captures complementary modalities such as hyperspectral imaging (HSI) and synthetic aperture radar (SAR), each encoding dis-

tinct physical properties. Effective fusion remains challenging due to differences across modalities [34]. Current approaches predominantly follow fully supervised paradigms; for example, recent methods like MSFMamba [38] focus on architectural advances. While these sophisticated architectures achieve competitive performance with abundant labeled data, they remain constrained by annotation requirements—a limitation particularly pronounced in practical remote sensing applications, where substantial geospatial variability exacerbates sparse annotations [26] and limits advanced supervised methods. In recent years, although large-scale labeled data have become available for multispectral and color satellite imagery [5, 11, 30, 32], advanced sensing modalities such as hyperspectral and SAR imaging do not yet have large-scale labeled datasets. Additionally, owing to the significant variability of sensor and acquisition specifications of advanced active and passive sensors, creating homogeneous large-scale labeled datasets for such modalities is not possible at present.

Additionally, foundation models such as SatMAE [6] and SpectralGPT [15] that employ masked autoencoder [12] architectures for multispectral data have shown promise, while GeodiffNet-F [17] demonstrates the potential of diffusion models for remote sensing classification. However, many of these approaches are largely limited to single modalities and cannot fully address the challenges posed by heterogeneous sensing modalities.

Diffusion models [13, 27, 28] offer a promising solution for multimodal fusion. Pretrained diffusion models achieve state-of-the-art performance in few-shot segmentation on natural images [2]. Unlike other self-supervised methods such as DINO [3], which struggle on textureless inputs, diffusion models leverage multi-scale noise training to capture spatial layouts effectively [37]. This allows them to extract meaningful features from challenging remote sensing data without relying on texture information [17]. Furthermore, their timestep conditioning mechanism [25] provides

a natural pathway for multimodal extension through joint timestep–modality conditioning, enabling unified processing of heterogeneous sensing modalities without separate encoders.

Direct application of ImageNet-pretrained diffusion models to remote sensing, however, faces substantial domain gaps. Existing cross-domain adaptation methods often require extensive parameter updates, increasing computational costs and risking catastrophic forgetting [19]. Parameter-efficient approaches such as LoRA [16] and DiffFit [33], while more efficient, rely on static modifications that may lack expressiveness for heterogeneous multimodal processing.

To address these challenges, we extend FiLM-based conditioning from semantic to sensor diversity, introducing joint timestep–modality conditioning that allows a single backbone to process multiple modalities and produce modality-specific features (e.g., HSI-optimized and SAR-optimized) while keeping the pretrained backbone frozen. Additionally, we propose a pseudo-RGB anchoring strategy to maintain alignment with ImageNet statistics during adaptation, mitigating catastrophic forgetting.

In summary, our contributions are:

1. **Unsupervised parameter-efficient multimodal adaptation.** We adapt a single ImageNet-pretrained diffusion model to heterogeneous modalities (HSI and SAR) using only unlabeled target data, updating just $\sim 5\%$ of parameters. The adapted model learns aligned multimodal representations within a shared backbone, enabling effective fusion under sparse supervision.
2. **Joint timestep–modality conditioning mechanism.** We extend diffusion conditioning from timestep-only to joint timestep–modality conditioning via FiLM layers that learn $\gamma(t, m)$ and $\beta(t, m)$. This enables dynamic, modality-specific feature extraction within a shared backbone while preserving pretrained generalization.
3. **Pseudo-RGB anchoring to prevent catastrophic forgetting.** Pseudo-RGB representations derived from HSI are used to preserve alignment with ImageNet statistics during adaptation. This anchoring mitigates catastrophic forgetting while enabling effective cross-modal feature learning.

2. Related Work

Multimodal Remote Sensing Fusion. Combining hyperspectral imaging (HSI) and synthetic aperture radar (SAR) improves land-cover classification by exploiting complementary spectral and structural cues. Early approaches such as FusAtNet [22], S²ENet [8], and DFNet [10] used CNN-based late fusion, while recent designs—AsyFFNet [39], ExViT [35], HCT [21], MACN [31], and MSFMamba [38]—incorporate attention

mechanisms, state-space blocks, and memory enhancements to capture long-range dependencies. Despite architectural advances, these methods remain predominantly fully supervised, constraining scalability when dense annotations are expensive across large geographical regions. This motivates pretrained approaches that reduce annotation dependence and improve generalization.

Pretrained Models in Remote Sensing. SatMAE [6] and SpectralGPT [15] adopt self-supervised masked autoencoders for multispectral imagery, while GeoDiffNet-F [17] leverages ImageNet-pretrained diffusion models for HSI classification. Such pretrained features enable processing at larger spatial scales without proportional annotation costs, but these methods remain single-modality. In particular, GeoDiffNet-F relies on converting HSI into pseudo-RGB representations, making extension to disparate modalities like SAR challenging due to their different sensor characteristics.

Diffusion Models for Feature Extraction. Pretrained diffusion models provide robust spatial representations for dense prediction tasks, showing strong performance even with limited labels [2]. They remain effective in challenging scenarios where other self-supervised methods may struggle [37]—a property especially relevant for remote sensing imagery with subtle or ambiguous textures, such as SAR or low-resolution multispectral data. Domain-specific efforts include DDPM-CD [1] for change detection and SpectralDiff [4] for HSI benchmarks, although training diffusion models from scratch is computationally expensive and constrained by dataset scale. Despite these challenges, leveraging ImageNet-pretrained diffusion models for multimodal fusion remains largely unexplored.

Parameter-Efficient Adaptation. Methods such as LoRA [9, 16] enable efficient adaptation through low-rank weight updates, while DiffFit [33] shows that updating a small subset of parameters—often normalization-related (e.g., scale and shift)—can yield effective domain adaptation. Recent work also demonstrates that diffusion model transferability varies across denoising timesteps, suggesting that adaptation strategies should account for these timestep-dependent differences [40]. These insights motivate our design of a joint timestep–modality conditioning scheme that adapts diffusion features efficiently without full fine-tuning.

FiLM and Adaptive Conditioning. Feature-wise Linear Modulation (FiLM) [25] introduced feature-wise affine conditioning, unifying concepts such as Conditional Batch Normalization and AdaIN [18]. Diffusion models leverage similar mechanisms: ADM employs Adaptive Layer Normalization for class conditioning [7], while DiT extends adaptive normalization to transformer backbones [24]. Building on this paradigm, we reinterpret class-conditioning pathways as modality-aware signals, enabling parameter-efficient adaptation for multimodal remote sens-

ing fusion.

3. Method

3.1. Problem Statement

We study the problem of adapting pretrained diffusion models for multi-source remote sensing pixel-level classification under sparse supervision.

Given multimodal inputs (HSI and SAR), we construct standardized 3-channel representations compatible with RGB-pretrained backbones: \tilde{X}_{pRGB} (HSI-derived pseudo-RGB via band selection), \tilde{X}_{PCA} (PCA-reduced HSI), and \tilde{X}_{SAR} (Pauli-decomposed SAR), as illustrated in Fig. 3 and Fig. 4.

This yields standardized inputs $\mathbf{X}^m \in \mathbb{R}^{H \times W \times 3}$, where $m \in \{\text{pRGB}, \text{PCA}, \text{SAR}\}$ indexes the representation type. Sparse supervision is available in the form of pixel-level labels:

$$\mathcal{Y} = \{(i, j, y_{ij}) : (i, j) \in \Omega\}, \quad (1)$$

where $|\Omega|$ accounts for less than 1% of pixels (0.97% for Augsburg and 0.61% for Berlin; see Tab. 1 and Tab. 2). **The goal is to classify each pixel into semantic land cover classes (e.g., forest, residential, industrial areas).**

Our objective is to leverage pretrained diffusion models for effective multimodal remote sensing classification under sparse supervision. To bridge the domain gap, we adapt them through parameter-efficient dynamic conditioning to extract representation-specific discriminative features while retaining the spatial priors learned from large-scale RGB pretraining.

3.2. Method Overview

Our approach consists of two stages: joint adaptation across representations followed by feature extraction and classification, as illustrated in Fig. 1.

Stage A – Joint Adaptation for Dense Feature Learning. We adapt a pretrained diffusion model to remote sensing data by repurposing its conditioning mechanism for representation-aware adaptation (see Sec. 3.3). Different noise levels require different adaptations: early timesteps (high noise) benefit from different transformations than late timesteps (low noise). We therefore generate conditioning parameters $\gamma(t, m)$ and $\beta(t, m)$ that jointly depend on timestep t and input representation $m \in \{\text{pRGB}, \text{PCA}, \text{SAR}\}$, allowing dynamic adaptation throughout the denoising process. All three representations are trained jointly, with HSI-derived pRGB used as an anchor to stabilize training (see Sec. 3.4). Importantly, this stage is parameter-efficient: only the lightweight conditioning networks are updated, while the large diffusion backbone remains frozen, as illustrated in Fig. 1.

Stage B – Feature Extraction and Classification. The adapted model, kept fully frozen, serves as a universal fea-

ture extractor. Pixel-wise classification is performed with fewer than 1% labeled data, without task-specific backbone training.

Key Distinction. Unlike static parameter-efficient methods (e.g., LoRA [16], DiffFit [33]) that apply fixed transformations, our timestep–representation conditioning adapts dynamically across both the denoising trajectory and input type, which is crucial for heterogeneous remote sensing data.

3.3. Modality-Aware Conditioning via Repurposed AdaGN

Modern diffusion models inject conditioning signals through Adaptive Group Normalization (AdaGN) layers [7] that apply scale–shift transformations:

$$\text{AdaGN}(h, c) = \gamma_c \cdot \text{GroupNorm}(h) + \beta_c. \quad (2)$$

We extend this FiLM-style conditioning mechanism [25] to incorporate modality information by introducing learned embeddings e_m for each representation type $m \in \{\text{pRGB}, \text{PCA}, \text{SAR}\}$:

$$\gamma(t, m) = \text{MLP}_\gamma(e_t + e_m), \quad (3)$$

$$\beta(t, m) = \text{MLP}_\beta(e_t + e_m), \quad (4)$$

where e_t is the timestep embedding. This joint conditioning enables dynamic, context-sensitive adaptation – i.e., each representation receives distinct normalization parameters that vary across denoising timesteps.

Novel Contribution. Existing diffusion approaches for remote sensing are typically trained from scratch for single modalities, while parameter-efficient adaptation methods (LoRA, DiffFit) apply static transformations that cannot account for heterogeneous sensor statistics. We introduce *joint timestep–modality conditioning*, extending diffusion conditioning from timestep-only $\gamma(t)$ to $\gamma(t, m)$ and $\beta(t, m)$ via FiLM layers. This enables dynamic adaptation that varies across both denoising timesteps and input modalities, allowing a single ImageNet-pretrained backbone to extract modality-specific features. Unlike static adaptation methods, which struggle with statistically divergent modalities (e.g., natural RGB-like HSI vs. synthetic aperture radar), our approach updates only $\sim 5\%$ of parameters through lightweight conditioning networks while keeping the pretrained backbone frozen, thus preserving learned spatial priors during multimodal adaptation.

Representation-Specific Feature Learning. The joint conditioning mechanism enables modality-specific normalization parameters within the shared backbone, supporting distinct transformations for each representation: pseudo-RGB preserves natural image statistics, PCA-reduced HSI captures spectral variations, and SAR accounts for synthetic aperture structures. This modality-aware adaptation

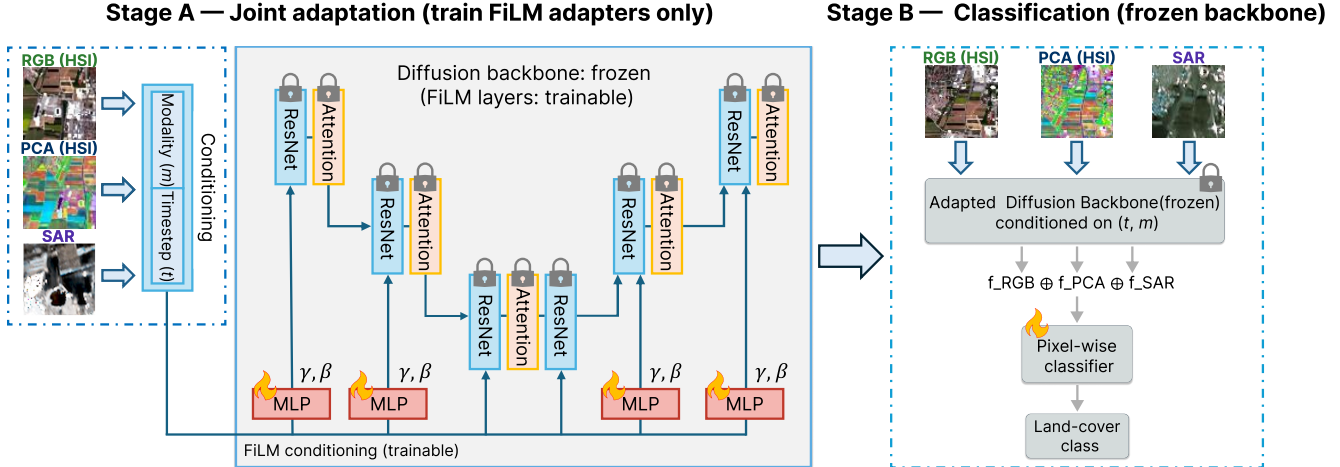


Figure 1. Two-stage parameter-efficient diffusion adaptation for multimodal remote sensing classification using ImageNet-pretrained models. Stage A: Joint adaptation using patch-based FiLM conditioning with pseudo-RGB anchoring. Stage B: Pixel-wise classification on co-registered multimodal features.

occurs while maintaining unified spatial processing through the frozen backbone, enabling effective cross-modal feature learning without separate encoders for each sensor type.

3.4. Anchor-Based Adaptation from Pretraining

Anchor-Based Drift Prevention. Diffusion models that process multiple modalities through a shared backbone are vulnerable to representation drift, where adaptation to divergent inputs can degrade performance below pretrained baselines. Although continual learning approaches mitigate forgetting by replaying prior task data [19], this is infeasible in our setting. Instead, we employ HSI-derived pRGB as an anchor, constraining drift while enabling domain-specific adaptation — a practical strategy for heterogeneous remote sensing modalities with divergent statistics.

Design Rationale. Pseudo-RGB serves a dual role: a processing modality (alongside PCA-reduced HSI and SAR) and a distributional anchor to ImageNet statistics. By leveraging the statistical similarity between HSI-derived pseudo-RGB and natural RGB images that ImageNet diffusion models were pretrained on, pseudo-RGB helps preserve alignment with pretrained spatial priors during adaptation. This stabilizing effect is particularly important when training jointly with statistically divergent modalities such as SAR, which lack RGB-like properties and otherwise risk inducing representation drift in the shared backbone.

The model is jointly trained using the diffusion denoising objective:

$$\mathcal{L}_{\text{denoise}} = \mathbb{E}_{x_0, t, m, \epsilon} \left[\|\epsilon - \epsilon_{\theta}(x_t, t, m)\|_2^2 \right], \quad (5)$$

where $m \in \{\text{pRGB}, \text{PCA}, \text{SAR}\}$ represents the three representations processed jointly, with pRGB providing distributional stability throughout adaptation.

3.5. Downstream Classification

Stage B: Frozen Feature Extraction. Following Stage A adaptation, the diffusion backbone remains frozen and serves as a feature extractor (Fig. 1, Stage B) that produces pixel-wise modality-specific features conditioned on both denoising timestep t and modality type $m \in \{\text{pRGB}, \text{PCA}, \text{SAR}\}$. During training, these conditioned features are used with sparse pixel-level annotations to supervise a lightweight classifier. At inference, the same conditioning mechanism enables dense prediction across all pixels for each of the three modality representations. This design ensures that performance reflects the representational quality gained through joint timestep–modality adaptation, rather than additional model capacity.

Classifier Architecture. A lightweight MLP head maps frozen diffusion features to pixel-wise class predictions. We freeze the backbone to avoid overfitting under sparse supervision, as fine-tuning large pretrained models in low-label regimes can degrade representations [20, 36]—a concern particularly pronounced in remote sensing where labeled data is scarce [29]. This approach isolates the representational gains from Stage A adaptation rather than additional model capacity, validating the effectiveness of our joint timestep–modality conditioning framework.

4. Experiments and Results

4.1. Datasets

We evaluate our approach on two established multimodal benchmarks that provide complementary evaluation scenarios across different sensor resolution regimes: **Augsburg** and **Berlin**. These datasets test our method’s robustness to different multimodal alignment strategies and spatial reso-

lution characteristics.

Augsburg (HSI: 180 bands, 332×485 pixels; SAR: VV/VH polarizations) represents a scenario where SAR data is downsampled to match coarser HSI resolution. Both modalities are co-registered to uniform 30 m GSD, with the original higher-resolution SAR aligned to the native HSI spatial grid. This configuration tests our joint conditioning approach when SAR spatial detail is reduced to enable fusion.

Berlin (HSI: 244 bands, 797×220 pixels; SAR: Sentinel-1 VV/VH) represents the opposite scenario where HSI is upsampled to match finer SAR resolution at 13.89 m GSD. The HSI data is resampled from its original 30 m resolution to the higher-resolution SAR spatial grid (final dimensions: $1723 \times 476 \times 244$), testing our approach when HSI spatial detail is interpolated for fusion.

Following benchmark protocols from Hong et al. [14], we use the official train–test splits to ensure comparability with recent multimodal fusion studies [38]. Both datasets exhibit severe class imbalance and label scarcity while providing dense pixel-level annotations (77,533 and 461,851 test pixels, respectively) that support comprehensive evaluation. This combination of dense annotations, class imbalance, and heterogeneous alignment provides a rigorous evaluation setting for sparse-label multimodal methods. Detailed class distributions are reported in Tab. 1 and Tab. 2.

Table 1. Augsburg dataset: training and testing pixel counts

Class	Train Count	Test Count
Forest	146	13,361
Residential Area	264	30,065
Industrial Area	21	3,830
Low Plants	248	26,609
Allotment	52	523
Commercial Area	7	1,638
Water	23	1,507
Total	761	77,533

Table 2. Berlin dataset: training and testing pixel counts

Class	Train Count	Test Count
Forest	443	54,511
Residential Area	423	268,219
Industrial Area	499	19,067
Low Plants	376	58,906
Soil	331	17,095
Allotment	280	13,025
Commercial Area	298	24,526
Water	170	6,502
Total	2,820	461,851

4.2. Implementation Details

Experimental Setup. All experiments are conducted on NVIDIA GeForce RTX 4080 GPUs using PyTorch 2.2 with CUDA 12.1. Random seeds are fixed for reproducibility.

Diffusion Backbone. We use the ADM (U-Net) model pretrained on 64×64 ImageNet images [7, 23]. The backbone remains frozen during adaptation, with only lightweight FiLM conditioning layers updated.

Training Protocol. We adopt a two-stage procedure: (i) domain adaptation using the Adam optimizer (lr=0.003) by updating only FiLM layers (batch size 32, 2000 steps) while keeping the diffusion backbone frozen, and (ii) MLP classifier training using Adam (lr=0.001, weight decay 5×10^{-4}) with batch size 64, 10 epochs, and early stopping. The classifier depth varies per dataset to match label set size.

Data Processing. Images are normalized using a 2nd–98th percentile stretch for all modalities: pseudo-RGB bands selected from HSI, the top three PCA components of HSI, and Pauli-decomposed SAR channels. The normalized images are then divided into 64×64 patches with 50% overlap (stride = 32). During inference, predictions from overlapping patches are merged by probability averaging to mitigate boundary artifacts.

Layer and Timestep Selection. We adopt the layer selection from GeoDiffNet-F [17] (layer 10 for Augsburg, layer 11 for Berlin) and determine timesteps through systematic ablation ($t = 0$ for Augsburg, $t = 300$ for Berlin). The corresponding ablation results that guided this choice are reported in Appendix B.

4.3. Main Results

We evaluate UniDiff on the Berlin and Augsburg multimodal datasets, benchmarking against recent baselines. Following prior work, we report per-class recall, overall accuracy (OA), average accuracy (AA), and Cohen’s kappa as the primary metrics; additional F1 and IoU results are provided in Appendix C.

Multimodal Performance. Tabs. 3 and 4 compare UniDiff with baselines in the HSI+SAR setting.

Berlin Dataset. UniDiff achieves 80.96% OA, 68.08% AA, and 70.05% Kappa, surpassing MSFMamba (76.92% OA, 64.88% AA, 64.88% Kappa) by +4.04% OA, +3.20% AA, and +5.17% Kappa, showing the effectiveness of our parameter-efficient adaptation strategy.

Augsburg Dataset. UniDiff reaches 93.08% OA, 71.68% AA, and 89.97% Kappa, outperforming MSFMamba (91.38% OA, 63.31% AA, 87.45% Kappa) by +1.70% OA, +8.37% AA, and +2.52% Kappa, confirming robustness across regions.

Scalability. In contrast to baselines constrained to fixed multimodal inputs, UniDiff accommodates both HSI-only and HSI+SAR configurations within a unified framework. For example, UniDiff achieves 74.96% OA on Berlin and 92.09% OA on Augsburg with HSI-only inputs (Appendix B), while further improving to 80.96% and 93.17% OA respectively when fusing HSI+SAR. This flexibility enables deployment under incomplete data conditions, avoid-

Table 3. Results on the **Berlin dataset** (per-class Recall). All methods are evaluated in the HSI+SAR multimodal setting. **UniDiff** shows consistent improvements over recent multimodal baselines. OA: Overall Accuracy, AA: Average Accuracy, Kappa: Kappa Coefficient (all reported in %).

Method	FusAtNet [22]	S ² ENet [8]	DFINet [10]	AsyFFNet [39]	ExViT [35]	HCT [21]	MACN [31]	MSFMamba [38]	UniDiff (Ours)
Forest	86.24	83.27	82.04	88.35	84.71	83.18	82.21	82.39	75.76
Residential	91.38	72.07	77.78	74.44	76.19	78.80	78.16	82.05	88.66
Industrial	19.76	46.66	47.96	48.21	44.15	43.59	47.79	48.91	57.53
Low Plants	20.00	72.08	77.78	71.41	77.96	76.48	78.04	79.72	85.55
Soil	48.72	77.94	87.85	80.75	67.13	82.92	77.26	85.22	89.00
Allotment	38.89	70.62	44.75	48.35	61.95	56.46	66.07	71.25	37.21
Commercial	18.47	36.48	29.85	27.97	29.28	18.96	28.90	31.08	34.32
Water	29.61	54.64	60.09	75.16	56.98	44.16	50.22	38.48	76.58
OA (%)	70.91	70.38	73.69	71.65	72.59	73.42	73.98	76.92	80.96
AA (%)	44.13	64.22	63.51	64.33	62.39	60.57	63.58	64.88	68.08
Kappa (%)	51.07	57.73	61.02	58.74	59.72	60.29	61.19	64.88	70.05

Table 4. Comparison on the **Augsburg dataset** (per-class Recall). **UniDiff (HSI+SAR)** achieves consistent improvements over recent multimodal baselines. OA: Overall Accuracy, AA: Average Accuracy, Kappa: Kappa Coefficient (all reported in %).

Method	FusAtNet [22]	S ² ENet [8]	DFINet [10]	AsyFFNet [39]	ExViT [35]	HCT [21]	MACN [31]	MSFMamba [38]	UniDiff (Ours)
Forest	94.34	98.10	97.38	97.56	90.04	97.26	97.84	97.17	97.28
Residential	92.56	99.08	98.37	99.16	95.44	98.63	98.73	98.15	97.87
Industrial	47.70	12.19	61.31	61.38	34.58	36.61	43.94	50.26	58.02
Low Plants	85.96	91.78	92.63	83.47	90.68	93.54	94.11	95.52	98.01
Allotment	49.33	45.12	49.33	42.64	51.82	51.43	52.39	53.35	85.47
Commercial	11.52	1.22	3.54	5.58	28.63	7.97	6.80	2.63	13.31
Water	45.27	24.09	26.61	45.81	17.65	46.34	48.54	49.97	51.82
OA (%)	85.31	88.12	90.66	88.25	86.65	90.33	91.06	91.38	93.08
AA (%)	62.93	53.08	61.31	62.23	58.41	61.68	63.19	63.31	71.68
Kappa (%)	86.33	86.47	86.47	83.13	80.79	86.03	87.06	87.45	89.97

ing the need to relearn modality relationships from scratch as in fully supervised methods.

Adaptation Stability Analysis. We examine performance across denoising timesteps to assess the effect of our joint condition adaptation. Fig. 2 shows mean F1 scores on the Berlin dataset, comparing adapted configurations with non-adapted counterparts that directly reuse ImageNet-pretrained features (Pre HSI and Pre HSI+SAR). Across timesteps 100–700, the adapted variants achieve consistently higher performance, with peak accuracy at timestep 300. These results suggest that adaptation provides clear and stable benefits over directly applying ImageNet-pretrained features, helping to mitigate the domain gap between natural images and multimodal remote sensing data. Comprehensive timestep analyses for both datasets are reported in Appendix B.

Qualitative Results. Figs. 3 and 4 present visual comparisons of classification maps. On Berlin, UniDiff reduces salt-and-pepper artifacts in urban areas; on Augsburg, water boundaries are more sharply delineated. Across both datasets, UniDiff preserves spatial detail while improving classification consistency.

4.4. Ablation Study

We conduct ablation experiments to assess the effectiveness of multimodal fusion, anchoring strategy, and parameter-

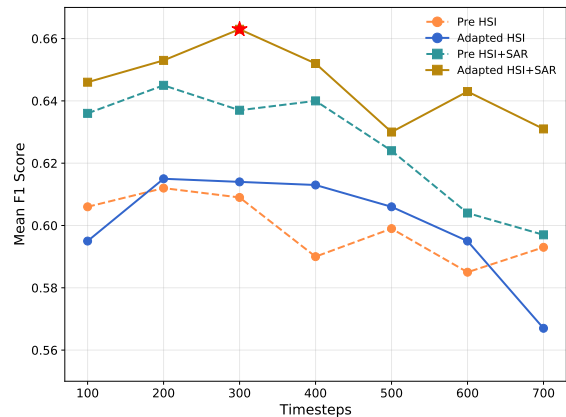


Figure 2. Adaptation benefits across denoising timesteps on the Berlin dataset (Mean F1 score). The adapted HSI+SAR configuration consistently outperforms pretrained baselines, with peak performance observed at timestep 300.

efficient adaptation.

Component Analysis (Berlin). Tab. 5 evaluates different modality combinations within our joint adaptation framework. Among individual representations, PCA achieves the best result (74.52% OA), followed by pRGB (73.31%)

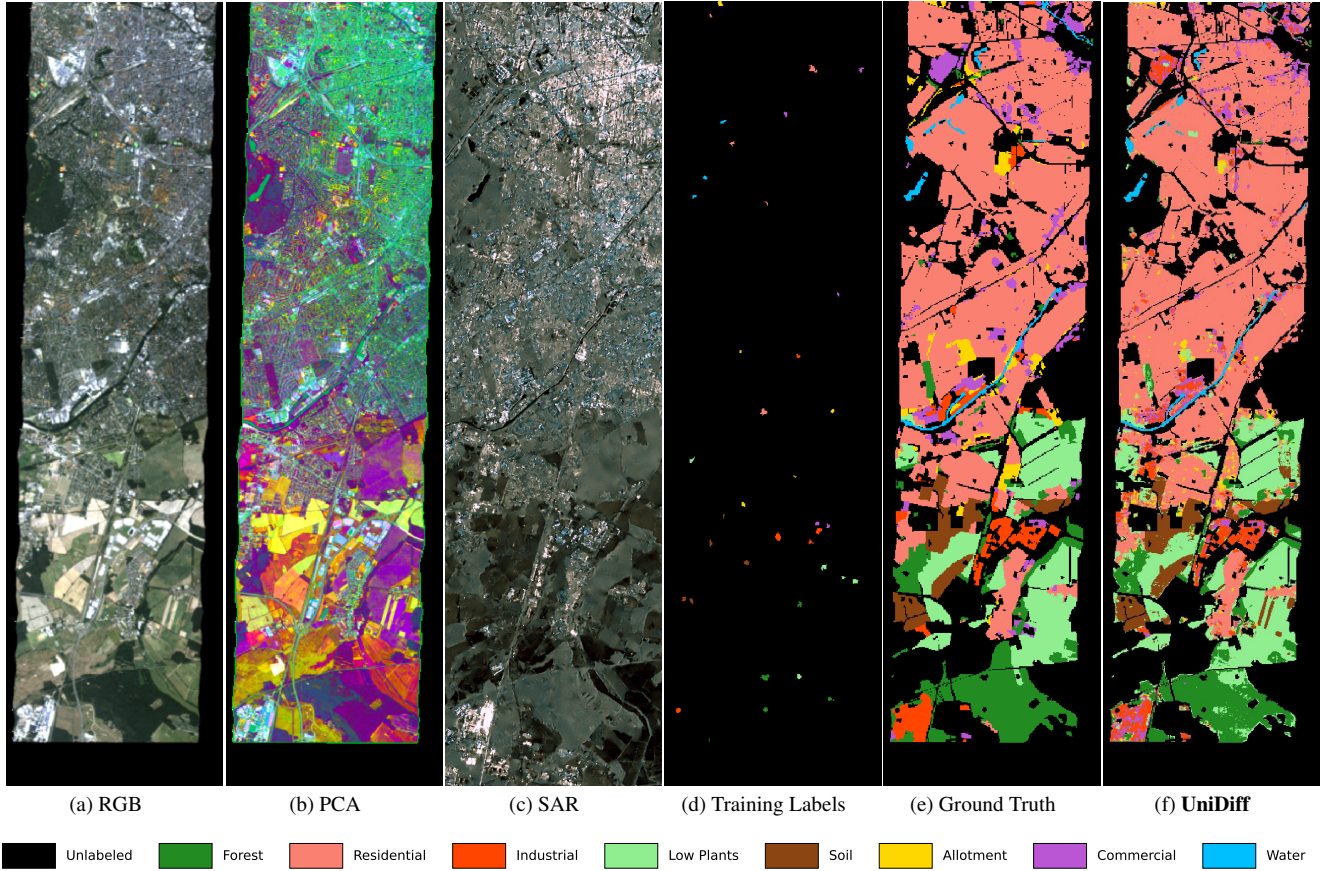


Figure 3. Visualization on the Berlin dataset with HSI and SAR. (a) Pseudo-RGB HSI, (b) PCA-reduced HSI, (c) SAR image, (d) Sparse Training Labels (limited pixel annotations provided in the benchmark), (e) Ground Truth, (f) UniDiff (ours, multimodal adaptation with HSI + SAR).

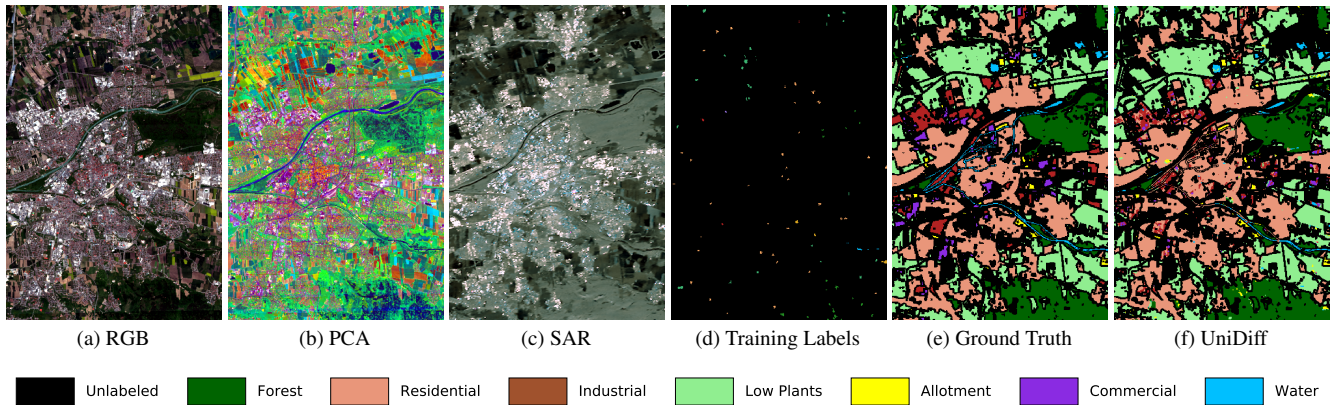


Figure 4. Visualization on the Augsburg dataset. Layout follows Fig. 3 (a-c) Input modalities, (d) sparse training labels, (e) ground truth, (f) UniDiff results.

and SAR (64.58%). That PCA surpasses pRGB despite lacking textures supports our claim that diffusion backbones leverage spatial layout rather than texture cues (see Sec. 1). Pairwise combinations show mixed outcomes:

adding SAR (pRGB+SAR, PCA+SAR at 75.03%) provides modest gains, while pRGB+PCA (72.97%) falls below PCA alone. The full pRGB+PCA+SAR configuration achieves the strongest performance (80.96% OA, 70.05%

Table 5. Component ablation on the Berlin dataset. Unsupervised joint adaptation with all modalities (pRGB, PCA, SAR), while evaluation is performed with different input combinations at test time. All metrics are reported in percentage. pRGB denotes pseudo-RGB from HSI bands.

Config	OA	KC	mF1	mIoU
pRGB	73.31	60.05	55.60	42.33
PCA	74.52	61.77	60.79	46.62
SAR	64.58	47.94	48.22	34.22
pRGB+PCA	72.97	60.74	61.65	47.93
pRGB+SAR	75.03	63.09	61.85	48.63
PCA+SAR	75.03	62.63	62.59	48.31
pRGB+PCA+SAR	80.96	70.05	66.25	53.34

KC, 66.25% mF1, 53.34% mIoU), confirming the benefit of complementary integration across modalities. Comprehensive per-class metrics and corresponding Augsburg results are provided in Appendix C.

Pseudo-RGB Anchoring Strategy. We evaluate the role of pseudo-RGB as both a domain anchor and a complementary information source. To isolate the anchoring effect, all methods are evaluated using only PCA features for classification. As shown in Tab. 6, PCA-only adaptation leads to catastrophic forgetting, performing worse than the pretrained baseline (69.59% vs 71.27% OA). This suggests that naive adaptation disrupts beneficial ImageNet priors, consistent with catastrophic forgetting [19]. In contrast, joint pRGB+PCA adaptation prevents this degradation and achieves the best results (74.96% OA, +5.37% over PCA-only). These results demonstrate that pseudo-RGB not only provides a complementary spatial HSI representation but also serves as an essential stabilizer during cross-modal adaptation, enabling more reliable pixel-wise classification.

Table 6. Pseudo-RGB anchoring ablation on Berlin (T300). All methods are evaluated with PCA features only. PCA-only trains on PCA; pRGB+PCA trains jointly but is tested on PCA.

Method	OA (%)	mF1 (%)	mIoU (%)
Pretrained (no adaptation)	71.27	58.89	43.88
PCA-only adaptation	69.59	57.20	42.88
pRGB+PCA joint adaptation	74.96	61.44	47.78
Δ vs PCA-only	+5.37	+4.24	+4.90

Parameter Efficiency Analysis. Our approach trains only lightweight adaptive layer norm MLPs ($\sim 5\%$ of total parameters) while keeping the diffusion backbone frozen. Despite this minimal parameter update, we achieve strong quantitative performance (80.96% OA on Berlin), demonstrating that pretrained ImageNet knowledge is effectively

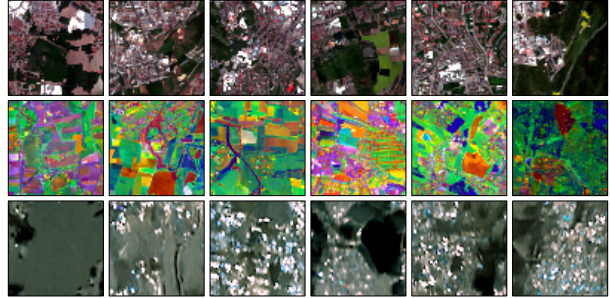


Figure 5. Representative patches generated after joint adaptation with only 5% trainable parameters. Rows show pseudo-RGB (top), PCA (middle), and SAR (bottom). The adapted model preserves modality-specific generative characteristics, demonstrating successful parameter-efficient domain adaptation.

preserved and leveraged rather than forgotten. Fig. 5 provides visual confirmation: the adapted model generates distinct, realistic patches for each modality—pseudo-RGB maintains natural image characteristics, PCA shows rich spectral patterns, and SAR exhibits appropriate structural features. Together, these quantitative and qualitative results validate that selective parameter updating enables effective domain adaptation without catastrophic forgetting of valuable pretrained priors.

4.5. Discussion

Cross-Modal Feature Organization. Joint adaptation induces systematic cross-modal organization with dataset-dependent patterns reflecting varying multimodal utility. Performance analysis highlights substantial differences in SAR contribution: Berlin gains +6.00% OA from HSI+SAR fusion, while Augsburg improves by only +1.08% (Appendix B). Cosine similarity analyses (Appendix D) reveal related organizational patterns—Berlin shows clearer pRGB–SAR separation, whereas Augsburg exhibits more complex reorganization. The most consistent effect across both datasets is reduced within-class variance in cross-modal similarities, indicating that joint adaptation yields more reliable feature relationships, independent of individual modality contribution levels.

Limitations. Our approach relies on empirically-determined adaptation stopping criteria and manual selection of diffusion parameters (timesteps and U-Net layers), which are validated across our datasets but may require re-tuning for different sensor modalities or tasks, reflecting broader methodological challenges in cross-modal adaptation and diffusion-based feature extraction. Developing adaptive strategies for stopping and parameter selection remains an exciting direction for future research. An anonymized implementation is provided at: <https://github.com/hutuhehe/UniDiff-code>.

References

- [1] Wele Gedara Chaminda Bandara, Nithin Gopalakrishnan Nair, and Vishal M Patel. Ddpm-cd: Denoising diffusion probabilistic models as feature extractors for change detection. *arXiv preprint arXiv:2206.11892*, 2022. 2
- [2] Dmitry Baranchuk, Ivan Rubachev, Andrey Voynov, Valentin Khruikov, and Artem Babenko. Label-efficient semantic segmentation with diffusion models. *arXiv preprint arXiv:2112.03126*, 2021. 1, 2
- [3] Mathilde Caron, Hugo Touvron, Ishan Misra, Hervé Jégou, Julien Mairal, Piotr Bojanowski, and Armand Joulin. Emerging properties in self-supervised vision transformers. In *Proceedings of the IEEE/CVF international conference on computer vision*, pages 9650–9660, 2021. 1
- [4] Ning Chen, Jun Yue, Leyuan Fang, and Shaobo Xia. Spectraldiff: A generative framework for hyperspectral image classification with diffusion models. *IEEE Transactions on Geoscience and Remote Sensing*, 61:1–16, 2023. 2
- [5] Kai Norman Clasen, Leonard Hackel, Tom Burgert, Gencer Sumbul, Begüm Demir, and Volker Markl. reben: Refined bigearthnet dataset for remote sensing image analysis. *arXiv preprint arXiv:2407.03653*, 2024. 1
- [6] Yezhen Cong, Samar Khanna, Chenlin Meng, Patrick Liu, Erik Rozi, Yutong He, Marshall Burke, David Lobell, and Stefano Ermon. Satmae: Pre-training transformers for temporal and multi-spectral satellite imagery. *Advances in Neural Information Processing Systems*, 35:197–211, 2022. 1, 2
- [7] Prafulla Dhariwal and Alexander Nichol. Diffusion models beat gans on image synthesis. *Advances in neural information processing systems*, 34:8780–8794, 2021. 2, 3, 5
- [8] Lu Fang, Sen Li, Yanfei Zhong, and Liangpei Zhang. S²enet: Spatial–spectral cross-modal attention network for hyperspectral and lidar data fusion. *IEEE Transactions on Geoscience and Remote Sensing*, 60:1–13, 2022. 2, 6
- [9] Rohit Gandikota, Joanna Materzyńska, Tingrui Zhou, Antonio Torralba, and David Bau. Concept sliders: Lora adaptors for precise control in diffusion models. In *European Conference on Computer Vision*, pages 172–188. Springer, 2024. 2
- [10] Yunhao Gao, Wei Li, Mengmeng Zhang, Jianbu Wang, Weiwei Sun, Ran Tao, and Qian Du. Hyperspectral and multispectral classification for coastal wetland using depthwise feature interaction network. *IEEE Transactions on Geoscience and Remote Sensing*, 60:1–15, 2021. 2, 6
- [11] Anatol Garioud, Nicolas Gonthier, Loic Landrieu, Apolline De Wit, Marion Valette, Marc Poupée, Sébastien Giordano, et al. Flair: a country-scale land cover semantic segmentation dataset from multi-source optical imagery. *Advances in Neural Information Processing Systems*, 36:16456–16482, 2023. 1
- [12] Kaiming He, Xinlei Chen, Saining Xie, Yanghao Li, Piotr Dollár, and Ross Girshick. Masked autoencoders are scalable vision learners. In *Proceedings of the IEEE/CVF conference on computer vision and pattern recognition*, pages 16000–16009, 2022. 1
- [13] Jonathan Ho, Ajay Jain, and Pieter Abbeel. Denoising diffusion probabilistic models. *Advances in neural information processing systems*, 33:6840–6851, 2020. 1
- [14] Danfeng Hong, Jingliang Hu, Jing Yao, Jocelyn Chanussot, and Xiao Xiang Zhu. Multimodal remote sensing benchmark datasets for land cover classification with a shared and specific feature learning model. *ISPRS Journal of Photogrammetry and Remote Sensing*, 178:68–80, 2021. 5
- [15] Danfeng Hong, Bing Zhang, Xuyang Li, Yuxuan Li, Chenyu Li, Jing Yao, Naoto Yokoya, Hao Li, Pedram Ghamisi, Xiuping Jia, et al. Spectralgpt: Spectral remote sensing foundation model. *IEEE Transactions on Pattern Analysis and Machine Intelligence*, 2024. 1, 2
- [16] Edward J Hu, Yelong Shen, Phillip Wallis, Zeyuan Allen-Zhu, Yuanzhi Li, Shean Wang, Lu Wang, Weizhu Chen, et al. Lora: Low-rank adaptation of large language models. *ICLR*, 1(2):3, 2022. 2, 3
- [17] Yuzhen Hu, Biplab Banerjee, and Saurabh Prasad. Label-efficient hyperspectral image classification via spectral film modulation of low-level pretrained diffusion features. In *TerraBytes-ICML 2025 workshop*, 2025. 1, 2, 5
- [18] Xun Huang and Serge Belongie. Arbitrary style transfer in real-time with adaptive instance normalization. In *Proceedings of the IEEE international conference on computer vision*, pages 1501–1510, 2017. 2
- [19] James Kirkpatrick, Razvan Pascanu, Neil Rabinowitz, Joel Veness, Guillaume Desjardins, Andrei A Rusu, Kieran Milan, John Quan, Tiago Ramalho, Agnieszka Grabska-Barwinska, et al. Overcoming catastrophic forgetting in neural networks. *Proceedings of the national academy of sciences*, 114(13):3521–3526, 2017. 2, 4, 8
- [20] Simon Kornblith, Jonathon Shlens, and Quoc V Le. Do better imagenet models transfer better? In *Proceedings of the IEEE/CVF conference on computer vision and pattern recognition*, pages 2661–2671, 2019. 4
- [21] Xiang Li, Liangpei Zhang, et al. Hct: Hyperspectral classification transformer using spectral–spatial tokens. *IEEE Transactions on Geoscience and Remote Sensing*, 60:1–12, 2022. 2, 6
- [22] Tanuj Mohla, Navreet Bhatia, Vikas Dhaka, and Ashok Kumar Dhaka. Fusatnet: Dual attention based spectro-spatial multimodal fusion network for hyperspectral and lidar classification. *IEEE Transactions on Geoscience and Remote Sensing*, 59(9):7491–7501, 2021. 2, 6
- [23] Alexander Quinn Nichol and Prafulla Dhariwal. Improved denoising diffusion probabilistic models. In *International conference on machine learning*, pages 8162–8171. PMLR, 2021. 5
- [24] William Peebles and Saining Xie. Scalable diffusion models with transformers. In *Proceedings of the IEEE/CVF international conference on computer vision*, pages 4195–4205, 2023. 2
- [25] Ethan Perez, Florian Strub, Harm De Vries, Vincent Dumoulin, and Aaron Courville. Film: Visual reasoning with a general conditioning layer. In *Proceedings of the AAAI conference on artificial intelligence*, 2018. 1, 2, 3
- [26] Farideh Foroozandeh Shahraki, Leila Saadatfard, Sebastian Berisha, Mahsa Lotfollahi, David Mayerich, and Saurabh

- Prasad. Deep learning for hyperspectral image analysis, part ii: Applications to remote sensing and biomedicine. In *Hyperspectral Image Analysis: Advances in Machine Learning and Signal Processing*, pages 69–115. Springer, 2020. [1](#)
- [27] Jascha Sohl-Dickstein, Eric Weiss, Niru Maheswaranathan, and Surya Ganguli. Deep unsupervised learning using nonequilibrium thermodynamics. In *International conference on machine learning*, pages 2256–2265. PMLR, 2015. [1](#)
- [28] Yang Song, Jascha Sohl-Dickstein, Durk P Kingma, Abhishek Kumar, Stefano Ermon, and Ben Poole. Score-based generative modeling through stochastic differential equations. *arXiv preprint arXiv:2011.13456*, 2020. [1](#)
- [29] Devis Tuia, Claudio Persello, and Lorenzo Bruzzone. Recent advances in domain adaptation for the classification of remote sensing data. *arXiv preprint arXiv:2104.07778*, 2021. [4](#)
- [30] Adam Van Etten and Daniel Hogan. The spacenet multi-temporal urban development challenge. *arXiv preprint arXiv:2102.11958*, 2021. [1](#)
- [31] Juncheng Wang, Li Zhang, Wei Li, et al. Macn: Multi-scale attention cross-modal network for hyperspectral and lidar data classification. *IEEE Transactions on Geoscience and Remote Sensing*, 61:1–15, 2023. [2](#), [6](#)
- [32] Junshi Xia, Naoto Yokoya, Bruno Adriano, and Clifford Broni-Bediako. Openearthmap: A benchmark dataset for global high-resolution land cover mapping. In *Proceedings of the IEEE/CVF Winter Conference on Applications of Computer Vision*, pages 6254–6264, 2023. [1](#)
- [33] Enze Xie, Lewei Yao, Han Shi, Zhili Liu, Daquan Zhou, Zhaoqiang Liu, Jiawei Li, and Zhenguo Li. Difffit: Unlocking transferability of large diffusion models via simple parameter-efficient fine-tuning. In *Proceedings of the IEEE/CVF International Conference on Computer Vision*, pages 4230–4239, 2023. [2](#), [3](#)
- [34] Xiaodong Xu, Wei Li, Qiangqiang Ran, Qian Du, Liang Gao, and Bing Zhang. Multisource remote sensing data classification based on convolutional neural network. *IEEE Transactions on Geoscience and Remote Sensing*, 56(2):937–949, 2018. [1](#)
- [35] Beibei Yao, Li Zhang, Wei Li, et al. Exvit: Explainable vision transformer for hyperspectral image classification. *IEEE Transactions on Geoscience and Remote Sensing*, 61:1–13, 2023. [2](#), [6](#)
- [36] Jason Yosinski, Jeff Clune, Yoshua Bengio, and Hod Lipson. How transferable are features in deep neural networks? *Advances in neural information processing systems*, 27, 2014. [4](#)
- [37] Junyi Zhang, Charles Herrmann, Junhwa Hur, Luisa Polania Cabrera, Varun Jampani, Deqing Sun, and Ming-Hsuan Yang. A tale of two features: Stable diffusion complements dino for zero-shot semantic correspondence. *Advances in Neural Information Processing Systems*, 36:45533–45547, 2023. [1](#), [2](#)
- [38] Wei Zhang, Jian Li, et al. Msfmamba: Multi-scale feature fusion state-space model for multi-source remote sensing classification. *IEEE Transactions on Geoscience and Remote Sensing*, 63:1–15, 2025. [1](#), [2](#), [5](#), [6](#)
- [39] Wei Zhao, Lei Gao, Wenjie Liao, and Aleksandra Pižurica. Asymmetric feature fusion network for hyperspectral and lidar classification. *IEEE Transactions on Geoscience and Remote Sensing*, 60:1–12, 2022. [2](#), [6](#)
- [40] Jincheng Zhong, Xingzhuo Guo, Jiaxiang Dong, and Mingsheng Long. Diffusion tuning: Transferring diffusion models via chain of forgetting. *Advances in Neural Information Processing Systems*, 37:114574–114600, 2024. [2](#)

Acknowledgments

We thank Ziyue Xu for error analysis, verification of geographic correspondence using mapping tools, and refinement of visual illustrations, which improved the clarity of the results presented in this work. We are especially grateful to the anonymous reviewer whose thoughtful guidance on broadening the scope and strengthening the validation helped clarify promising future directions for this work. We also thank the other reviewers for their insightful and constructive feedback.